Time-Resolved Electromagnetic Near-Field Scanning: Dual Sparse Sampling in Time and Space

Yanming Zhang , *Member, IEEE*, Peifeng Ma , *Senior Member, IEEE*, Lijun Jiang , *Fellow, IEEE*, and Steven Gao , *Fellow, IEEE*

Abstract—Time-resolved electromagnetic near-field scanning plays a pivotal role in antenna measurement and unraveling complex electromagnetic interference and compatibility issues. However, the rapid acquisition of high-resolution spatio–temporal data remains challenging due to physical constraints, such as moving the probe position and allowing sufficient time for sampling. This article presents a novel hybrid approach combining Kriging for sparse spatial measurement, compressed sensing (CS) for sparse temporal sampling, and dynamic mode decomposition (DMD) for comprehensive analysis of the dual-sparse sampling electromagnetic near-field data. We leverage CS to optimize sparse sampling in the time domain and Latin hypercube sampling to guide the probe position and realize sparse measurement in the space domain. By leveraging the inherent sparsity within electromagnetic radiated signals, CS reliably represents time-domain signals while reducing the required time samples. Then, DMD is used to extract meaningful insights from the resulting sparse spatio–temporal data, resulting in the sparse dynamic modes and temporal evolution information. Next, the Kriging is employed to infer missing spatial measurements for each sparse dynamic mode. Finally, the entire spatio–temporal signals are reconstructed based on interpolated dynamic modes and temporal evolution information. An example using crossed dipole antennas as the device under test is provided to validate the proposed method. It is found that the proposed Kriging-CS-DMD framework effectively reconstructs electromagnetic fields with precision while simultaneously reducing the measurement workload in both the time and space domains. This methodology could be further employed for various applications, such as space–time-modulated electronic devices.

Index Terms—Compressed sensing (CS), dynamic mode decomposition (DMD), electromagnetic near-field scanning, Kriging, time-resolved measurement.

Yanming Zhang and Steven Gao are with the Department of Electronic Engineering, Chinese University of Hong Kong, Shatin, Hong Kong (e-mail: ymzhang@cuhk.edu.hk; scgao@ee.cuhk.edu.hk).

Peifeng Ma is with the Department of Geography and Resource Management, Institute of Space and Earth Information Science, Chinese University of Hong Kong, Shatin, Hong Kong (e-mail: mapeifeng@cuhk.edu.hk).

Lijun Jiang is with the Department of Electrical and Computer Engineering, Missouri University of Science and Technology, Rolla, MO 65409 USA (e-mail: ljf82@mst.edu).

I. Introduction

ELECTROMAGNETIC (EM) near-field scanning, as a critical tool, provides invaluable support for antenna measurement [1], [2], [3] and the comprehensive investigation of complex EM interference and EM compatibility phenomena [2], [4], [5]. However, obtaining radiation distribution in EM near-field scanning is still a challenging task because it consumes a significant amount of time during the process of data acquisition [6]. In particular, it is customary to move sensing probes to different positions to capture EM field data in the target area during the near-field scanning [7]. This process entails the physical displacement of the probes, a task that can be notably time-consuming when collecting data from numerous pixels [8], [9], [10]. Accordingly, this drawback becomes particularly pronounced when striving for high resolution, making it imperative to develop a method for quickly acquiring EM near-field scanning data [11], [12].

Several methods have been developed to accelerate data acquisition in the context of near-field scanning. These methods, including sequential sampling [6], compressed sensing (CS) [13], equilateral-triangular-spaced samples [14], Kriging method [9], and wide-mesh scanning [15], are primarily centered around spatially sparse sampling in the frequency domain. Subsequently, the data acquired through these sparse sampling techniques reconstruct the corresponding global spatial distributions at each frequency. Recently, to enhance the measurement and analysis of transient EM phenomena, the time-domain distribution measurements in EM near-field scanning have been introduced, as discussed in previous works [16], [17], [18], [19]. In contrast to the traditional frequency-domain measurements carried out using spectrum analyzers or vector network analyzers, the time-domain near-field scanning approach involves acquiring electrical signals through high-speed oscilloscopes. Subsequently, time-varying field signals are deduced through basic computational process [20], [21]. Effectively capturing time-varying near-field distributions necessitates simultaneously sampling both temporal and spatial dimensions. This requirement introduces fresh complexities when conducting high-speed near-field scanning. It is imperative to consider the synchronization and coordination of temporal and spatial sampling methodologies to accurately characterize transient EM phenomena.

In this article, we propose a hybrid method, Kriging-CS-DMD, that combines Kriging, CS, and dynamic mode

decomposition (DMD) to address the challenges posed by temporal and spatial sampling in near-field scanning. Specifically, CS is utilized to achieve temporal sparsity in data acquisition, whereas Latin hypercube sampling facilitates spatial sparse sampling. Subsequently, the resulting spatio–temporal dual-sparse data are subjected to DMD analysis, allowing us to extract sparse dynamic modes and corresponding frequency information. Then, the Kriging method is used to recover the full dynamic modes from the sparse dynamic modes. Finally, the proposed hybrid approach reconstructs original spatio–temporal field distributions based on the full dynamic modes and the corresponding frequency information. Our work is motivated by the demand for more efficient near-field EM field measurements. We introduce a sparse sampling technique that optimally reduces measurement time while maintaining data quality, ideal for applications with limited time and resources. To summarize, the main highlights of this work are as follows.

1) In the time domain, we employ CS to optimize temporal sampling. By exploiting the inherent sparsity in EM signals, CS significantly reduces the number of required time samples, making time-domain data acquisition more efficient and cost effective.

2) We leverage Kriging, a spatial interpolation technique, to enhance spatial measurement efficiency by inferring missing spatial data points. This reduces the need for exhaustive spatial sampling, making space-domain data acquisition more resource efficient and faster.

3) To extract meaningful insights from the resulting sparse spatio–temporal data, we utilize DMD, a powerful technique for identifying sparse dynamic modes, capturing temporal evolution, and providing reconstruction of entire spatio–temporal field distributions. It is worth noting that DMD, as a spatio–temporally correlated decomposition algorithm, enables the Kriging method to be applied to a few sparse dominant modes rather than sparse field distributions at every time step, thereby expediting the recovery of complete spatio–temporal data.

The rest of this article is organized as follows. Section II offers a detailed exposition of the Kriging-CS-DMD methodology. In Section III, we present a numerical case study to evaluate the efficacy of our proposed approach. Section IV presents discussion. Finally, Section V concludes this article.

II. METHODOLOGY

This section commences by introducing the application of CS to analyze temporally sparse sampling, the Kriging method for spatially sparse sampling analysis, and the DMD approach for analyzing spatio–temporal data. Subsequently, a comprehensive exposition is provided on the Kriging-CS-DMD methodology.

A. CS and Temporally Sparse Sampling

Without loss of generality, consider the scenario where a time-domain signal, denoted by $\mathbf{p}^t \in \mathbb{R}^m$, is acquired through near-field scanning by a probe positioned at a fixed location. This signal can be related to another vector, $\mathbf{s}$, which is K-sparse in a specific basis $\mathbf{B} \in \mathbb{R}^{m \times m}$. This relationship is mathematically expressed as follows:

$$\mathbf{p}^t = \mathbf{B}\mathbf{s} \tag{1}$$

where $\mathbf{s}$ is a vector with exactly K nonzero elements, and $K \ll m$. When $\mathbf{p}^t$ exhibits this K-sparsity within the basis $\mathbf{B}$, it opens the possibility to acquire a subset of measurements instead of directly measuring $\mathbf{p}^t$ in time-resolved near-field scanning.

Subsequently, we collect a subset of time-domain measurements denoted as $\mathbf{q}^t \in \mathbb{R}^n$, where $K < n \ll m$. These measurements are represented by

$$\mathbf{q}^t = \mathbf{C}\mathbf{p}^t. \tag{2}$$

Herein, the matrix $\mathbf{C} \in \mathbb{R}^{n \times m}$ corresponds to n linear measurements performed on the state vector $\mathbf{p}^t$. Assuming that we have knowledge of the sparse vector $\mathbf{s}$, it becomes feasible to reconstruct the complete state vector $\mathbf{p}^t$ using (1). Thus, we can solve the following system of equations to determine $\mathbf{s}$, given the measurements $\mathbf{q}^t$ and having information about the sparse basis $\mathbf{B}$ and the measurement matrix $\mathbf{C}$:

$$\mathbf{q}^t = \mathbf{C}\mathbf{B}\mathbf{s}. \tag{3}$$

This sparse sampling system allows us to recover the original state vector $\mathbf{p}^t$ by utilizing the measured data $\mathbf{q}^t$ in conjunction with the sparse basis $\mathbf{B}$ and the measurement matrix $\mathbf{C}$. Thus, the objective of this reconstruction is to identify the sparsest solution $\hat{\mathbf{s}}$ that satisfies the optimization problem defined as follows:

$$\hat{\mathbf{s}} = \underset{\mathbf{s}}{\operatorname{argmin}} \|\mathbf{s}\|_0, \text{ subject to } \mathbf{q}^t = \mathbf{C}\mathbf{B}\mathbf{s}. \tag{4}$$

Herein, $\|\mathbf{s}\|_0$ represents the count of nonzero elements in $\mathbf{s}$. Notably, the effectiveness of this approach relies on two key conditions. 1) The measurement matrix $\mathbf{C}$ should exhibit incoherence with respect to the basis $\mathbf{B}$, indicating that the rows of $\mathbf{C}$ are uncorrelated with the columns of $\mathbf{B}$, and 2) a sufficient number of measurements, on the order of $\mathcal{O}(K \log(m/K))$, must be collected. The specific constant factor depends on the level of incoherence between $\mathbf{C}$ and $\mathbf{B}$ [22]. These conditions ensure that the matrix product $\mathbf{C}\mathbf{\Psi}$ satisfies the restricted isometry property (RIP) for K-sparse vectors $\mathbf{s}$, given as follows [23]:

$$(1 - \delta_K) \|\mathbf{s}\|_2^2 \leq \|\mathbf{C}\mathbf{B}\mathbf{s}\|_2^2 \leq (1 + \delta_K) \|\mathbf{s}\|_2^2 \tag{5}$$

where δ_K denotes the restricted isometry constant. The RIP property implies that $\mathbf{C}\mathbf{B}$ acts as a nearly unitary transformation on K-sparse vectors, preserving relative distances.

To satisfy the RIP for reliable signal reconstruction from the solution of (4), we adopt the Gaussian random measurement matrices for the sampling matrices $\mathbf{C}$ and Fourier basis for $\mathbf{B}$. The choice to utilize Gaussian random measurement matrices is primarily grounded in its practicality [24]. Specifically, sampling at random point locations offers a high degree of convenience, providing an effective means of signal acquisition in the context of near-field scanning. Furthermore, the Fourier basis of $\mathbf{B}$ is a generic basis. A noteworthy benefit is the inherent incoherence exhibited by single-point measurements in relation to this basis [25]. It is worth noting that to ensure sufficient degrees of freedom for estimating $\mathbf{s}$ when the dynamics of the source

are unknown, it is advised to select $\mathbf{B}$ based on its efficiency in representing a broad range of signals using the Fourier. The choice of $\mathbf{C}$ as a Gaussian random matrix promotes incoherence with $\mathbf{B}$, essential for CS effectiveness. Increasing measurement numbers relative to the sparsity of $\mathbf{s}$ further aids in achieving stable and accurate signal reconstruction.

Once the matrices $\mathbf{C}$ and $\mathbf{B}$ have been determined, we could be ready to proceed with the solution of (4). Regrettably, the optimization problem presented in (4) is nonconvex and can only be tackled via a brute-force search. The computational complexity of this search is combinatorial in terms of m and K, rendering it a nonpolynomial time problem. Consequently, solving (4) becomes infeasible, even for moderately large values of m and K. It is fortunate that the greedy algorithms can be used to determine the sparse solution of (4). Herein, the CS matching pursuit is employed for its easy-to-implement and computationally efficient [26].

B. Kriging Method and Spatially Sparse Sampling

The Kriging method, also recognized as Gaussian process regression, embodies nonparametric probabilistic models reliant on kernels [9], [27]. Initially conceived within the domain of geology and mining [27], this statistical modeling approach has seen diverse applications, encompassing reconstruction of EM fields [9], [16], [28], [29]. In our approach, the Kriging method plays a central role in spatially sparse sampling by informing the probe's movement during near-field scanning. This geostatistical technique enables us to predict unknown field values from a limited number of measurements, thus optimizing the spatial distribution of sampling points. Specifically, when addressing the challenge of 2-D planar near-field scanning, we consider the global field, denoted by $\mathbf{p}_s \in \mathbb{R}^{r_1 \times r_2}$, to exist within a spatial dimension of $r_1 \times r_2$. However, due to the inherent limitations in measurement resources and time, we collect data from only Z spatial sampling points, where $Z \ll (r_1 \times r_2)$, significantly less than the total number of points in the spatial grid.

It is assumed that Z sampling points are selected by the Latin hypercube sampling theory. Then, Kriging formulates the following expression based on the coordinates of these Z sampling points and the collected field values:

$$\mathbf{p}_s^{\text{Kri}}(\mathbf{r}) = \sum_{i=1}^{I} \beta_i h_i(\mathbf{r}) + \sum_{z=1}^{Z} \alpha_z \phi(\theta, \mathbf{r}_z, \mathbf{r}) \qquad (6)$$

where the coefficients β_i and α_z are obtained via a generalized least-squares procedure. The initial segment of (6) can be viewed as a linear regression with respect to the basis functions $h_i(\mathbf{r})$. Typically, these basis functions are chosen to be low-order polynomials or constants [16]. The latter part of (6) signifies a localized deviation from the regression component, represented as a summation of Z-shifted instances of the correlation function, each centered on an individual data sample [16]. Considering the characteristics of near-field patterns, the adoption of a Gaussian correlation function emerges as an appropriate choice, as

outlined below:

$$\phi(\theta, \mathbf{r}_z, \mathbf{r}) = \prod_{j=1}^{J} e^{-\theta_j \left| \mathbf{r}_z^{(j)} - \mathbf{r}^{(j)} \right|^2}. \qquad (7)$$

Herein, the index j is employed to iterate over all coordinates of the probe, which are stored in the vector $\mathbf{r}$. Maximum likelihood estimation is used here to estimate the parameters θ_j [30], [31].

C. Dynamic Mode Decomposition

DMD originated from fluid dynamics [32] and has subsequently been widely applied in other fields, such as chaotic signal processing [33], [34], orbital angular momentum wave detection [35], [36], [37], source localization techniques [38], [39], [40], and so on. In the following, we will discuss how to perform DMD analysis based on global spatio–temporal data in this section, while the next section will cover DMD analysis and reconstruction based on spatio–temporal doubly sparse data.

To commence the DMD analysis, we initially focus on the entire spatio–temporal data acquired from time-resolved near-field scanning, denoted as $\mathbf{P} \in \mathbb{R}^{R \times m}$. Herein, the variable R represents the total number of pixels comprising the entire field, where R is the product of r_1 and r_2. In addition, the parameter m corresponds to the total number of sampled points in the temporal domain. These are consistent with the previous symbols. In preparation for the application of DMD, the collected data have been partitioned into two distinct data matrices, as delineated below:

$$\mathbf{P}_R^1 = [\mathbf{p}_R^1, \mathbf{p}_R^2, \dots, \mathbf{p}_R^k, \dots, \mathbf{p}_R^{m-1}] \qquad (8)$$

$$\mathbf{P}_R^2 = [\mathbf{p}_R^2, \mathbf{p}_R^3, \dots, \mathbf{p}_R^k, \dots, \mathbf{p}_R^m] \qquad (9)$$

where $\mathbf{p}_R^k$ means the field distribution at time k. The subscript R indicates the number of spatial sampling points, the superscript represents the number of temporal sampling points, and k denotes the index for the temporal sampling.

Subsequently, it is posited that a linear mapping connection exists between successive states, formulated as $\mathbf{p}_R^{k+1} = \mathbf{F}(\mathbf{p}_R^k)$. The correspondence between the two sets of temporally shifted snapshots, as illustrated in (8) and (9), can be effectively characterized by employing the mapping matrix denoted as $\mathbf{M}$. This characterization can be succinctly expressed as follows:

$$\mathbf{P}_R^2 = \mathbf{M}_R \mathbf{P}_R^1. \qquad (10)$$

In this context, the mapping matrix $\mathbf{M}_R$ encapsulates the intricate dynamic patterns exhibited by the radiated EM field. Within the framework of DMD, the determination of principal eigenvalues and their corresponding eigenvectors within $\mathbf{M}$ can be computed using a singular value decomposition (SVD)-based approach [41], [42]. To be specific, the first step entails employing the SVD to represent the matrix $\mathbf{P}_R^1$ as follows:

$$\mathbf{P}_R^1 = \mathbf{U}_R \mathbf{S}_R \mathbf{V}_R^* \qquad (11)$$

where $*$ signifies the conjugate transpose operation. By substituting the pseudoinverse of (11) into (10) through a right-multiplication operation, we obtain

$$\mathbf{M}_R = \mathbf{P}_R^2 \mathbf{V}_R \mathbf{S}_R^{-1} \mathbf{U}_R^*. \qquad (12)$$
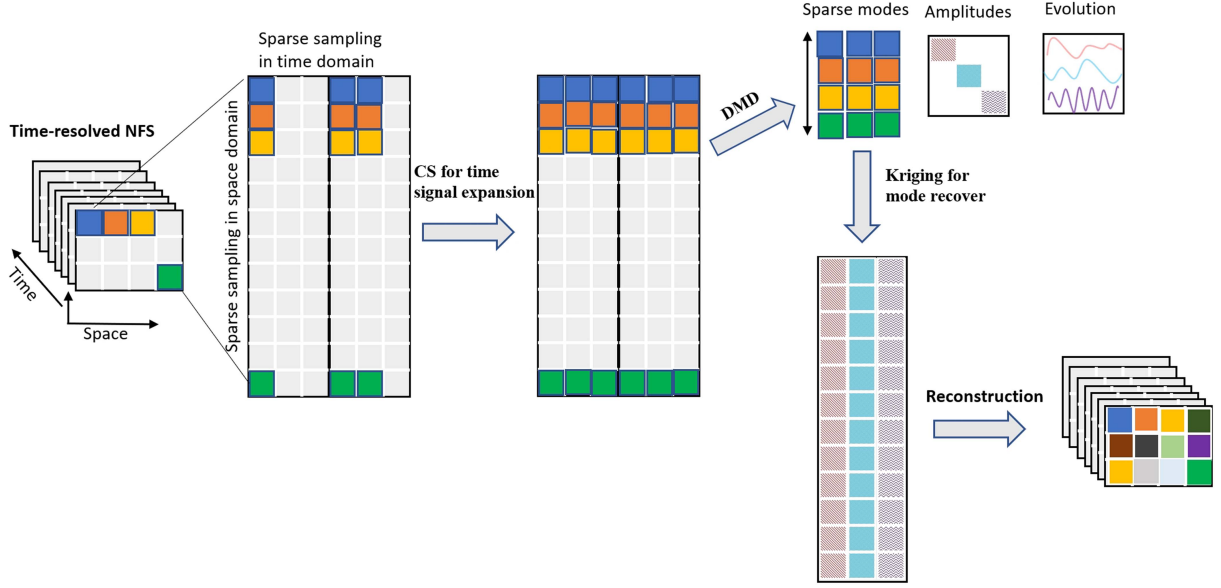
Fig. 1. Schematic of the proposed Kriging-CS-DMD for near-field scanning with dual sparse sampling in both time and space domains.

Then, the original states in (10) are projected into a low-rank system by using the matrix $\mathbf{U}_R$, namely, $\widehat{\mathbf{P}}_R^1 = \mathbf{U}_R^* \mathbf{P}_R^1$, $\widehat{\mathbf{P}}_R^2 = \mathbf{U}_R^* \mathbf{P}_R^2$, and $\widehat{\mathbf{M}}_R = \mathbf{U}_R^* \mathbf{M}_R \mathbf{U}_R$. Herein, the notation $\widehat{(\cdot)}$ is utilized to denote all the representations within the newly established low-rank system. Subsequently, the eigendecomposition of $\widehat{\mathbf{M}}_R$ is computed to capture the main dynamic characteristics, which is given as follows:

$$\widehat{\mathbf{M}}_R \mathbf{A}_R = \mathbf{A}_R \mathbf{\Gamma} \qquad (13)$$

where the columns of matrix $\mathbf{A}_R$ represent the eigenvectors, while the diagonal elements of the matrix $\mathbf{\Gamma}$, denoted as γ_l with $l = 1, 2, \ldots, L$, signify the eigenvalues. Consequently, the construction of the dynamic mode in the original state proceeds as follows:

$$\mathbf{Y} = \mathbf{P}_R^2 \mathbf{V}_R \mathbf{S}_R^{-1} \mathbf{A}_R. \qquad (14)$$

Finally, the DMD approach furnishes a comprehensive model for the observed entire radiated EM field within near-field scanning, which is given as follows:

$$\mathbf{p}_R(t) = \sum_{l=1}^{L} \mathbf{y}_l \exp(\omega_l t)\beta_l = \sum_{l=1}^{L} \mathbf{y}_l \exp(\omega_l^{\text{real}} t + j\omega_l^{\text{imag}} t)\beta_l. \qquad (15)$$

Straightforwardly, the original signal representation $\mathbf{p}_R(t)$ is expressed as a linear combination of dynamic modes $\mathbf{y}_l$, characterized by their respective damping factor and frequency information, denoted as $\omega_l = \omega_l^{\text{real}} + j\omega_l^{\text{imag}} = \frac{\ln(\gamma_l)}{\delta t}$, and amplitude coefficients β_l. Notably, the DMD method formulates this governing equation for the radiated field solely based on the available observed entire data. Subsequently, we will elucidate how DMD can be applied to analyze sparse data and model the entire field based on dual spatio–temporal sparse sampling.

D. Kriging-Compressed Sensing-Dynamic Mode Decomposition

Fig. 1 illustrates the steps of the proposed Kriging-CS-DMD method for the EM near-field scanning, particularly in situations where both spatial sampling and temporal sampling are sparse. This method aims to provide a comprehensive representation of the EM field by leveraging a multistep process.

Step 1) Dual sparse sampling: The initial step involves a sparse sampling process that yields a limited number of spatial data points (Z) and discrete time samples (n). The spatial points are carefully selected based on the Latin hypercube sampling strategy, and the temporal samples are obtained randomly at these locations. Thus, the obtained spatio–temporal data are denoted as $\mathbf{Q}_Z^n \in \mathbb{R}^{Z \times n}$. The selection of n must satisfy (5) in the context of CS, and the choice of Z should be at least greater than the square root of the desired resolution. In addition, this is related to the spatial correlation of the field.

Step 2) Temporal signal expansion: To enhance the temporal resolution of the sparse data, the CS matching pursuit [26] is used. Based on (4), this technique increases the number of time samples (n) by generating and obtaining m contiguous time samples at each of the Z spatial points. The result is a denser and more informative temporal dataset, which is denoted as $\mathbf{Q}_Z^m \in \mathbb{R}^{Z \times m}$.

Step 3) Dynamic mode decomposition: The dataset $\mathbf{Q}_Z^m$ with $Z \times m$ data points is subjected to DMD analysis. DMD extracts sparse dynamic modes from this data, revealing the underlying patterns and behaviors in both the spatial and temporal dimensions. Based on (15), DMD can model $\mathbf{Q}_Z^m$ as follows:

$$\mathbf{q}_Z(t) = \sum_{l=1}^{L} \mathbf{x}_l \exp(\eta_l t)\alpha_l = \sum_{l=1}^{L} \mathbf{x}_l \exp(\eta_l^{\text{real}} t + j\eta_l^{\text{imag}} t)\alpha_l \qquad (16)$$

where $\mathbf{q}_Z(t)$ means the time-varying state in the sparse spatial domain. $\mathbf{x}_l$ means the sparse dynamic modes, which capture the key sparse spatial features of the EM radiated fields. η_l^{real} and η_l^{imag}, respectively, means the damping factor and frequency information. α_l means the corresponding amplitude weights. In a comparative analysis between (15) and (16), it can be seen that (15) involves DMD analysis applied to the entire spatio–temporal signal, whereas (16) employs DMD on a spatially sparse signal. Importantly, the spatial dimension of the sparse dynamic modes in (16) is noticeably smaller than that of the entire signal, namely, $Z \ll R$. Since the temporal dimension information has been reconstructed through CS, it is theoretically expected to be correlated between α_l and β_l. This correlation is contingent upon the effectiveness of the CS recovery process. In other words, the better the results obtained from the CS recovery, the more consistent the outcomes in the temporal dimension processing.

Step 4) Modes recover via the Kriging method: Subsequently, the Kriging method is applied to recover the complete global dynamic modes from the sparse dynamic modes. Based on (7), the Kriging process increases the representation from the sparse Z spatial dimensions, i.e., $\mathbf{x}_l \in \mathbb{R}^Z$, to the complete R spatial dimensions, i.e., $\mathbf{x}_l^{\text{Kri}} \in \mathbb{R}^R$. It is worth noting that each sparse dynamic mode is individually recovered, and thus, their respective associations with frequencies remain unchanged. In other words, the recovered distributions, $\mathbf{x}_l^{\text{Kri}}$, can be considered as the spatial profiles corresponding to each frequency component.

Step 5) Reconstruction: Then, $\mathbf{x}_l^{\text{Kri}}$ is used to replace the $\mathbf{x}_l$ in (16). The entire spatio–temporal radiated fields can be modeled as follows:

$$
\begin{aligned}
\mathbf{q}_R(t) &= \sum_{l=1}^{L} \mathbf{x}_l^{\text{Kri}} \exp(\eta_l t)\alpha_l \\
&= \sum_{l=1}^{L} \mathbf{x}_l^{\text{Kri}} \exp(\eta_l^{\text{real}}t + j\eta_l^{\text{imag}}t)\alpha_l.
\end{aligned}
\tag{17}
$$

Clearly, the notable advantage of the Kriging-CS-DMD approach is its ability to construct a data-driven model for time-resolved near-field scanning only based on the doubly sparse data. This enables the reconstruction of entire distributions, the identification of frequency components, and the determination of their corresponding spatial distributions. The method serves as a valuable tool for gaining comprehensive insights into time-varying EM field behavior, particularly in scenarios characterized by limited and sparse sampling in both spatial and temporal dimensions.

III. RESULTS

A. Utilizing Crossed Dipole Antennas as the Device Under Test (DUT)

To verify the proposed Kriging-CS-DMD methodology, we conduct a simulation experiment utilizing the crossed dipole antennas [43] as the DUT, whose configuration is shown, as illustrated in Fig. 2. This setup consists of a 5-GHz dipole antenna oriented along the x-axis and a 2.4-GHz dipole antenna oriented
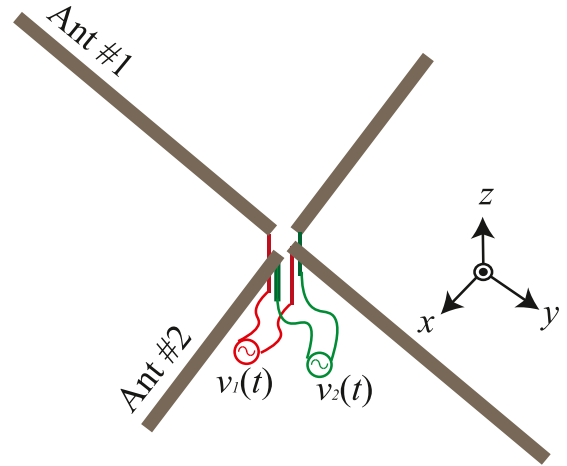

Fig. 2. Crossed dipole antenna with two different exciting signals.

along the y-axis. The selection of these specific frequencies is made to align with the operational frequencies of WiFi 5 and WiFi 6 [44], ensuring the relevance of our investigation to contemporary wireless communication standards. Herein, both antennas are configured as half-wave dipole antennas. Antenna #1 operates at the 2.4-GHz frequency band ($\lambda_1 = 0.125$ m), whereas Antenna #2 is designed for the 5-GHz frequency band ($\lambda_2 = 0.06$ m). Sinusoidal waves, denoted as $v_1(t)$ and $v_2(t)$, are used to excite Antenna #1 and #2, respectively, operating at 2.4 and 5 GHz, respectively. The scanning plane is accurately positioned at a fixed distance of 0.3 m above the crossed dipole antenna. This positioning strategy is chosen to effectively capture the near-field region characteristics of the DUT's radiative behavior. The time-resolved near-field scanning results were obtained using the 4NEC2 [45], [46] software.

Fig. 3 illustrates the magnitude of the electric field in the z-direction, represented as E_z, at three specific time points: namely, 2, 4, and 5 ns. These results demonstrate that the electric field varies over time, emphasizing the time-varying nature of the radiation emission process. In practical measurements, obtaining the data depicted in the figure involves the sampling of 256×256 spatial points and 1000 points in the 10 ns time dimension. This results in a substantial amount of data that need to be collected, amounting to $256 \times 256 \times 1000$ points in total. Such data acquisition is time-consuming, particularly when it involves physically moving probes and waiting for an adequate number of samples in the time dimension.

To address the issue of extended sampling times in the time-resolved near-field scanning system, we have implemented a sparsity-based sampling approach in both the spatial and temporal domains. The specific temporal and spatial sparsity strategies are detailed in Sections III-B and III-C, respectively. Subsequently, we employ the DMD algorithm to analyze and reconstruct the data collected through dual sparse sampling. This allows us to obtain comprehensive information about the entire time-varying radiation, as well as the spatial distribution corresponding to each frequency. A detailed explanation of this process can be found in Section III-D.
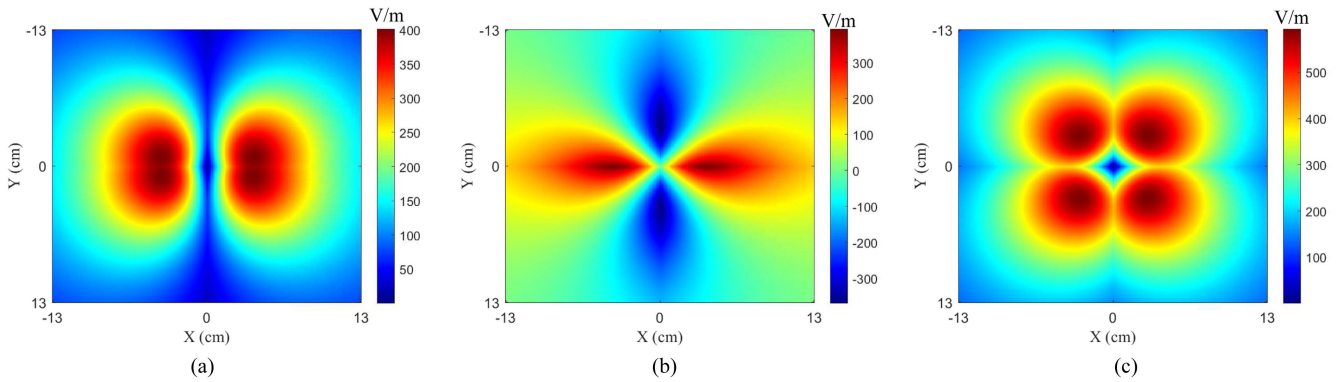
Fig. 3. Simulated time-resolved near-field scanning results for the crossed dipole antenna: the spatial distribution of electric field E_z at (a) 2, (b) 4, and (c) 5 ns.
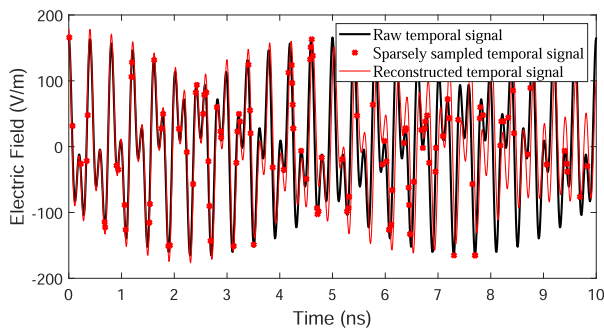

Fig. 4. Time-domain sparsity sampling and reconstruction results: original time-domain data (1000 points, black solid line), sparse sampled points (128 points, red dots), and reconstructed time signal obtained via CS.

Fig. 5. Power spectrum of (a) original time-domain data and (b) reconstructed signal.

B. Sparse Sampling in Time Domain

To validate the sparse sampling in the time domain, we began by selecting an arbitrary spatial pixel as an example. With a sampling rate of 0.01 ns within a 10 ns window, we acquired a total of 1000 time samples. For sparse sampling, 128 points were chosen among these samples. Herein, we apply the CS technique to perform sparse sampling and subsequent signal recovery in the time domain. In Fig. 4, the original time-domain data, represented by a black solid line consisting of 1000 data points, are shown alongside the sparsely sampled points depicted as red dots, amounting to 128 data points. Then, the CS process reconstructs the original signal based on the 128 data points. Fig. 4 presents the corresponding results of reconstruction. It can be seen that 1000 data points have been successfully recovered and exhibit consistency with the original signal.

To further compare, we compute the power spectrum of both the original and reconstructed signals. Fig. 5(a) and (b) illustrates the power spectrum of the original and rebuilt signals, respectively. The original and rebuilt signals exhibit a high degree of consistency, with both the 2.4 and 5 GHz frequencies clearly extracted. This means that the reconstructed signal effectively recovers the frequency characteristics present in the original signal, demonstrating its reliability in preserving the signal's frequency features. Hence, the CS technique effectively rebuilds the full-time signal with high reliability from the sparse samples,
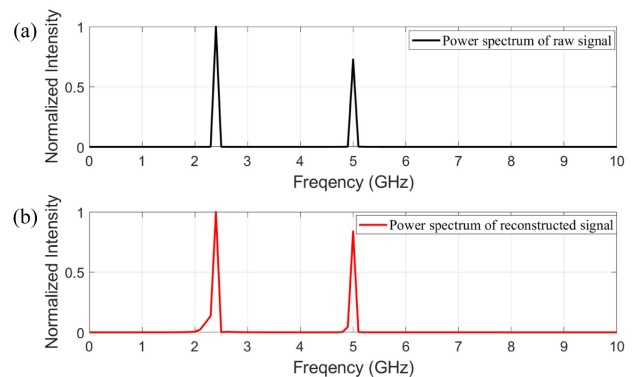
demonstrating the power of CS in efficiently acquiring and reconstructing data while significantly reducing the required sampling effort.

C. Sparse Sampling in Space Domain

We employ Kriging to carefully select spatial sampling points with sparsity, resulting in reduced sample requirements and more efficient measurements. Initially, we adopt Latin hypercube sampling [47], [48] during positioning spatial sampling points in the near-field scanning. This approach enables us to select measurement points across the spatial area of interest judiciously. Unlike random sampling, Latin hypercube sampling guarantees a more uniform distribution of sampling points. This characteristic proves especially beneficial for characterizing EM fields [48]. Fig. 6(a)–(c) depicts the selection of sparse points using Latin hypercube sampling, with corresponding sample counts of 300, 500, and 800 points, respectively. Subsequently, we utilize the Kriging model for reconstruction. Fig. 6(d)–(f) represents the corresponding reconstruction results. As the number of sampling points increases, the reconstruction quality improves, aligning with the intuition. We use peak signal-to-noise ratio (PSNR) as a measure for these reconstructions. The PSNR values for reconstructions with 300, 500, and 800 sampling points are 3.4778, 3.5019, and 3.5049 dB, respectively. These results indicate that the reconstruction error decreases as the number
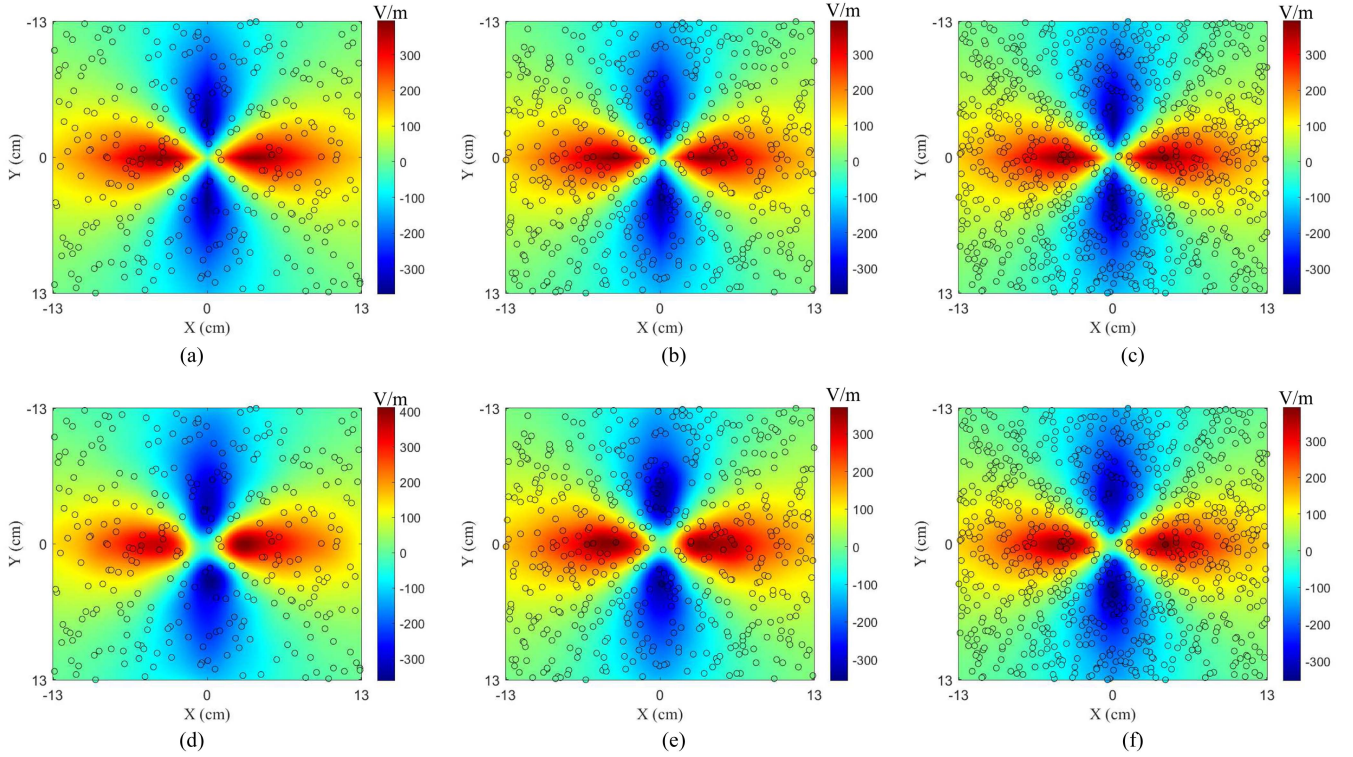
Fig. 6.   Spatial sparsity sampling diagram: data sample distribution for (a) 300, (b) 500, and (c) 800 samples, and their respective reconstruction results in (d)–(f).

of sampling points increases, leading to better reconstruction outcomes. It is worth noting that its applicability may vary across different types of field sources, depending on their inherent spatial correlations. The choice of sample points follows the Latin hypercube sampling principle, necessitating a minimum of one sample per dimension for the desired image resolution. This approach is flexible, varying according to the field characteristics, measurement surface, and frequency, with the optimal number of samples tailored to the resolution and specific spatial correlations. Next, we integrate sparse sampling in both time and space domains and introduce the Kriging-CS-DMD method to analyze and reconstruct data acquired through dual sparse sampling. Detailed information regarding this is elaborated in the following section.

D. Dual Sparse Sampling and Analysis Via Kriging–CS–DMD

As illustrated in Fig. 4, sparse sampling in the time domain is depicted, wherein the initial number of sampled data points is 1000. Utilizing CS, this quantity is effectively reduced to 128 data points. Consequently, the temporal sparse sampling factor equates to approximately 7.8 times. Furthermore, Fig. 6 portrays the scenario of sparse sampling in the spatial domain. In this context, the original pixel count for sampling corresponds to 256×256. Employing the Kriging method, 500 pixels are chosen for reconstruction, resulting in a spatial sparse sampling factor of approximately 131, demonstrating the efficiency of our sampling strategy for a 256×256 resolution space. It is evident that the synergy of temporal and spatial sparse sampling

is instrumental in the overall reduction of data dimensionality and contributes to the efficiency of the data acquisition process.

Next, we conduct an analysis of data acquired through dual sparse sampling using the Kriging-CS-DMD framework. Through the Kriging-CS-DMD analysis of dual sparse sampled data, we obtain the DMD spectrum, depicted in Fig. 7(b). For comparison, we also calculate the DMD spectrum obtained via the raw data analysis, shown in Fig. 7(a). The value indicated by the black dotted line corresponds to the measurement along the horizontal axis. Clearly, the DMD and Kriging-CS-DMD analyses successfully extract two distinct frequency components, 2.4 and 5.0 GHz, which align closely with the actual scenario. Hence, this high degree of concordance between these two sets of results shows that Kriging-CS-DMD can extract frequency information of the radiation field using temporally and spatially doubly sparse sampled data.

Furthermore, we have visualized the corresponding dynamic modes in Fig. 8, alongside the representation of the original modes for the sake of comparison. We take the 2.4 GHz dynamic mode as an example, which is plotted in Fig. 8(b). Herein, the black circles represent sampling points, and based on these 500 sampling points, we reconstruct the entire field data. For comparison, we also show the actual radiation mode in Fig. 8(a). It is clear that they are consistent with each other. The same finding can be obtained in 5.0 GHz, and the results are shown in Fig. 8(c) and (d). Hence, we can conclude that the Kriging-CS-DMD method can also derive the spatial radiation pattern of each frequency based on the temporally and spatially doubly sparse sampled data. These collective results underscore
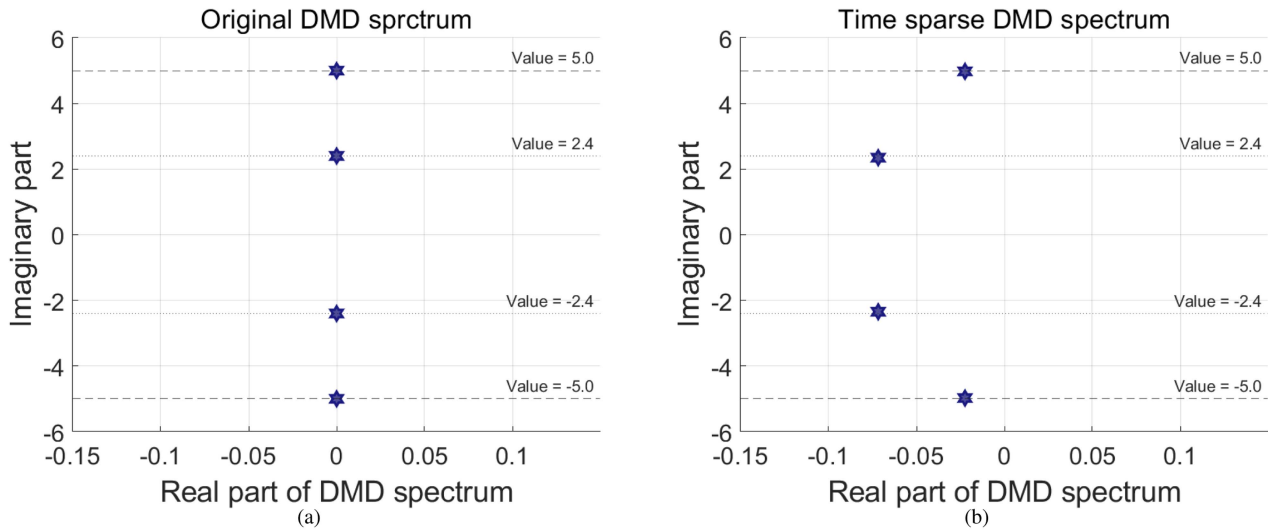
Fig. 7. (a) DMD spectrum acquired through the utilization of DMD for the analysis of the original dataset. (b) DMD spectrum obtained by employing the Kriging-CS-DMD for the analysis of spatio–temporal dual sparse data.
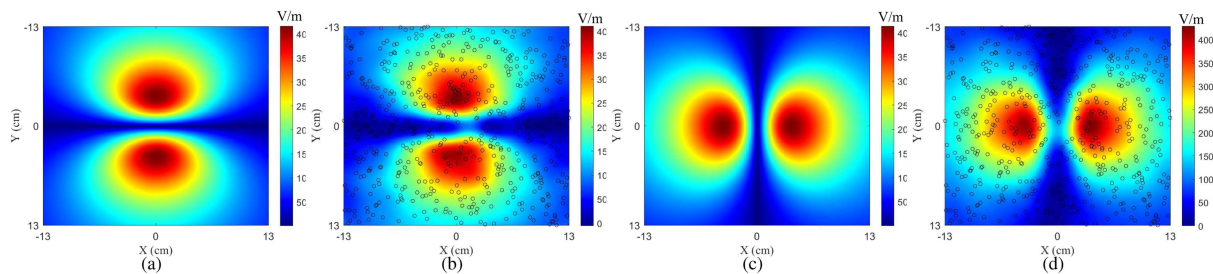

Fig. 8. (a) Raw radiated filed distribution at 2.4 GHz. (b) 2.4 GHz mode extracted by Kriging-CS-DMD method. (a) Raw radiated filed distribution at 5.0 GHz. (b) 5.0 GHz mode extracted by Kriging-CS-DMD method.

the efficacy of the Kriging-CS-DMD framework in extracting essential frequency information and elucidating the associated spatial distribution.

Fig. 9 shows the raw spatial distribution of the electric field E_z and the reconstruction result of the electric field E_z at three different times, i.e., 2, 4, and 5 ns. Herein, we employ 2 ns as an example for explanation. Fig. 9(a) shows the actual radiated field with a resolution of 256×256 pixels. Fig. 9(b) plots the CS reconstruction with temporal sparse sampling (128 points). Notably, it can be observed that the CS reconstruction effectively recovers the temporal variations, utilizing data obtained through temporal sparse sampling, albeit with some distortion. Fig. 9(c) illustrates the Kriging reconstruction with spatial sparse sampling (500 pixels), demonstrating this method's effectiveness in recovering data based on spatial sparse sampling. Fig. 9(d) and (e) shows the Kriging-CS-DMD reconstruction using temporally and spatially doubly sparse sampled data. In Fig. 9(d), 128 temporal sampling points and 500 spatial sampling pixels are employed, while in Fig. 9(e), 128 temporal sampling points and 1000 spatial sampling pixels are used. It is evident that, based on temporally and spatially doubly sparse data, the Kriging-CS-DMD method efficiently restores the global distribution. Furthermore, the noise introduced during the CS

TABLE I
COMPARISON OF PSNR OF THE RECONSTRUCTION RESULT WITH DIFFERENT SNRS AT $t = 2$ NS SHOWN IN FIG. 9

SNR	PSNR
Noise free	24.9294 dB
40 dB	22.4729 dB
30 dB	19.0053 dB
20 dB	15.8350 dB
10 dB	9.4455 dB

reconstruction is mitigated due to the rank-reduction computation within DMD. Comparing Fig. 9(d) and (e), it is apparent that with an increased number of spatial sampling points, the reconstructed field closely approximates the real distribution, aligning with intuitive expectations. This observation holds true across different time points. Hence, we conclude that Kriging-CS-DMD is capable of extracting both the frequency components and their corresponding spatial distributions from doubly sparse fields, resulting in the reconstruction of the global distribution.

Table I presents a comparison of PSNR values corresponding to the quality of EM field reconstruction results at different signal-to-noise ratios (SNRs) at a specific time point ($t = 2$).
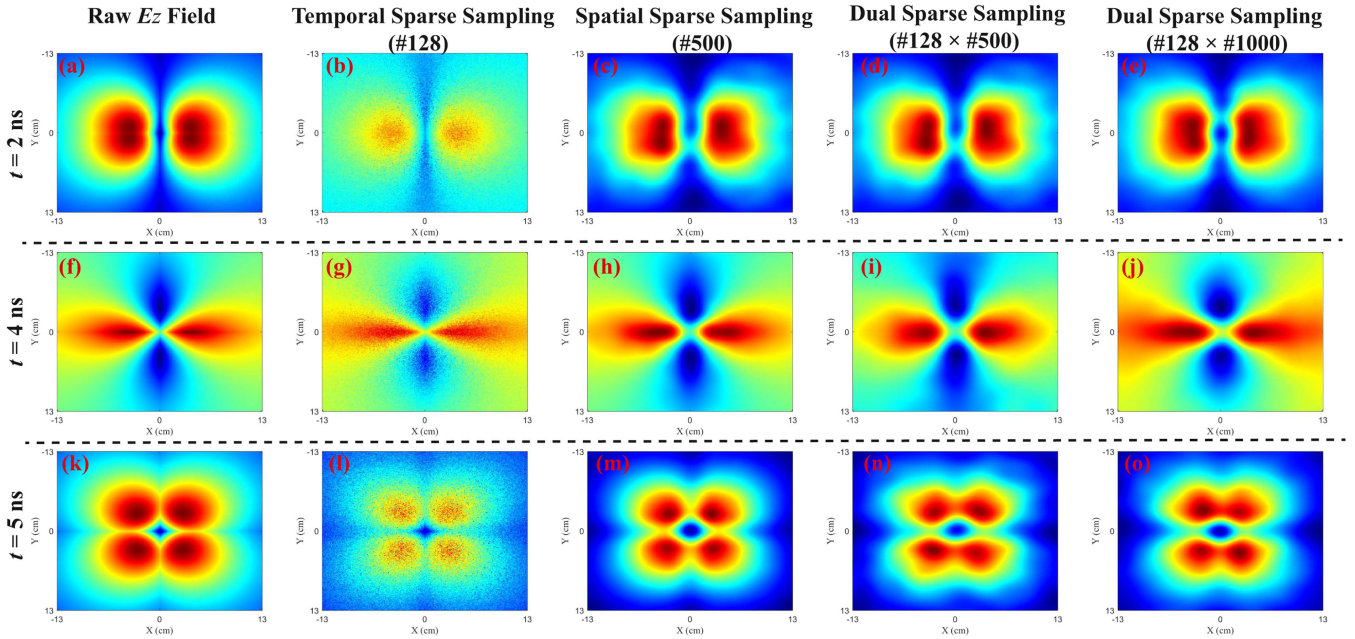
Fig. 9.   Raw spatial distribution of electric field E_z and reconstruction results at different time points. (a) Raw radiated field (256×256 pixels) at 2 ns. (b) CS reconstruction with temporal sparse sampling (128 points) at 2 ns. (c) Kriging reconstruction with spatial sparse sampling (500 pixels) at 2 ns. (d) Kriging-CS-DMD reconstruction with temporally and spatially doubly sparse sampled data (128 temporal points and 500 spatial pixels) at 2 ns. (e) Kriging-CS-DMD reconstruction with temporally and spatially doubly sparse sampled data (128 temporal points and 1000 spatial pixels) at 2 ns. (f) Raw radiated field (256×256 pixels) at 4 ns. (g) CS reconstruction with temporal sparse sampling (128 points) at 4 ns. (h) Kriging reconstruction with spatial sparse sampling (500 pixels) at 4 ns. (i) Kriging-CS-DMD Reconstruction with temporally and spatially doubly sparse sampled data (128 temporal points and 500 spatial pixels) at 4 ns. (j) Kriging-CS-DMD reconstruction with temporally and spatially doubly sparse sampled data (128 temporal points and 1000 spatial pixels) at 4 ns. (k) Raw radiated field (256×256 pixels) at 5 ns. (l) CS reconstruction with temporal sparse sampling (128 points) at 5 ns. (m) Kriging reconstruction with spatial sparse sampling (500 pixels) at 5 ns. (n) Kriging-CS-DMD reconstruction with temporally and spatially doubly sparse sampled data (128 temporal points and 500 spatial pixels) at 5 ns. (o) Kriging-CS-DMD reconstruction with temporally and spatially doubly sparse sampled data (128 temporal points and 1000 spatial pixels) at 5 ns.

The PSNR is a measure of the reconstruction's fidelity, higher values indicate a closer approximation to the original, noise-free signal. In noise-free conditions, the reconstruction achieves the highest PSNR of approximately 24.93 dB, indicating a high-quality reconstruction. As the SNR decreases from 40 to 10 dB, there is a corresponding decrease in PSNR values, indicating that the presence of noise adversely affects the quality of the reconstruction. At an SNR of 40 dB, the PSNR remains high at around 22.47 dB, suggesting that the method is still robust at this level of noise. However, as the noise level increases, the PSNR drops to around 19.01 dB at 30 dB SNR, 15.84 dB at 20 dB SNR, and to a lower value of 9.45 dB at 10 dB SNR, highlighting a significant degradation in reconstruction quality in higher noise environments. While the DMD algorithm employs SVD to differentiate the signal from noise under low-noise conditions, its effectiveness diminishes as noise intensifies, resulting in decomposition inaccuracies and adversely affecting the EM field reconstruction indicated by the mapping matrix $\mathbf{M}_R$ in (10). The effectiveness of noise reduction through truncated SVD might not suffice, particularly in cases with high noise levels.

IV. DISCUSSION

By distinguishing between the sampling methods applied across the time and space domains, namely, random sampling for temporal measurements and Latin hypercube sampling (LHS)

for spatial measurements, we leverage the strengths of both strategies. Random sampling in the time domain captures the dynamic nature of EM fields with fewer samples, whereas LHS in the spatial domain ensures comprehensive and efficient coverage of the scanning area, thereby optimizing the overall measurement process. This approach, combining spatial measurements guided by LHS and temporal measurements facilitated by a high-speed oscilloscope, effectively satisfies the dual requirements for sparse sampling in both domains. It allows us to reconstruct the EM field with high fidelity, capitalizing on the sparsity inherent in the field's spatial and temporal characteristics. Besides, by employing LHS for spatial points and random sampling for the temporal domain, our method allows synchronization of sample capture at these spatial points over time. This negates the need for multiple oscilloscopes and resource-heavy setups, ensuring efficient and accurate EM field reconstruction.

Table II depicts the comparison between the proposed method and several existing near-field scanning methods, including sequential sampling-based method [5], [49], CS-based method [13], [50], and conjugate gradient method [51]. The proposed method for near-field scanning represents a significant advancement over existing techniques by offering comprehensive sparse sampling in both the time domain and space domain. This dual-domain sparse sampling is crucial for efficient data acquisition in complex EM field environments, where the sheer volume of data can be overwhelming and the fine details are

TABLE II
COMPARISON BETWEEN THE PROPOSED METHOD AND SEVERAL EXISTING NEAR-FIELD SCANNING METHODS

Feature	Sequential sampling [5], [49]	CS [13], [50]	Conjugate gradient method [51]	Proposed method
Time-domain scanning	×	✓	×	✓
Frequency-domain scanning	✓	✓	✓	×
Sparse spatial sampling	✓	✓	✓	✓
Temporal spatial sampling	×	✓	×	✓
Spatial temporal correlation	×	×	×	✓

critical for accurate analysis. Also, the unique capability of the proposed method to analyze spatial–temporal correlation sets it apart from other methods listed in the table. This feature underlines the method's sophisticated analytical power, offering insights into the dynamic interplay between spatial and temporal variations in the EM field.

V. CONCLUSION

In this section, we introduced the Kriging-CS-DMD approach for addressing the challenges associated with dual temporal and spatial sampling in near-field scanning. We have optimized data acquisition by leveraging Kriging for spatial sparse sampling and compressed sensing for achieving temporal sparsity while maintaining data fidelity. Applying DMD to the resulting spatio–temporal dual-sparse data has allowed us to extract valuable insights, including frequency information and global spatial distributions for each frequency. Our numerical case study has demonstrated the proposed method's efficiency and accuracy in reconstructing EM fields while reducing measurement overhead. This methodology could be adopted in various applications, particularly in space–time-modulated electronic device scenarios.

REFERENCES

[1] A. Tatsuta, S. Tanimoto, S. Fujino, T. Miyai, S. Nakamura, and S. Yagitani, "Development of 2D near field scanner for electromagnetic noise visualization," in *Proc. IEEE Symp. Electromagn. Compat. Signal/Power Integrity*, 2023, pp. 448–453.

[2] S. Voskresenskyi, I. Aitbar, E. Ballukja, K. Niewiadomski, D. W. P. Thomas, and S. Greedy, "State of the art of near-field scanning: Contemporary standards and methods," in *Proc. IEEE 7th Glob. Electromagn. Compat. Conf.*, 2023, pp. 29–30.

[3] D. Wang, X.-C. Wei, E.-X. Liu, and R. X.-K. Gao, "Probe design and source reconstruction for near-field scanning and modeling," *IEEE Electromagn. Compat. Mag.*, vol. 12, no. 1, pp. 75–86, Jan.–Mar. 2023.

[4] J. Fan, "Near-field scanning for EM emission characterization," *IEEE Electromagn. Compat. Mag.*, vol. 4, no. 3, pp. 67–73, Jul.–Sep. 2015.

[5] S. Serpaud, A. Boyer, S. B. Dhia, and F. Coccetti, "Efficiency of sequential spatial adaptive sampling algorithm to accelerate multifrequency near-field scanning measurement," *IEEE Trans. Electromagn. Compat.*, vol. 64, no. 3, pp. 816–826, Jun. 2022.

[6] S. Serpaud, A. Boyer, S. Ben-Dhia, and F. Coccetti, "Fast and accurate near-field measurement method using sequential spatial adaptive sampling (SSAS) algorithm," *IEEE Trans. Electromagn. Compat.*, vol. 63, no. 3, pp. 858–869, Jun. 2021.

[7] K.-L. Chen, Y. Guo, J. Wang, and X. Yang, "Contactless islanding detection method using electric field sensors," *IEEE Trans. Instrum. Meas.*, vol. 70, 2021, Art. no. 9001413.

[8] F. R. Varela, B. G. Iragüen, and M. Sierra-Castaner, "Application of nonuniform FFT to spherical near-field antenna measurements," *IEEE Trans. Antennas Propag.*, vol. 68, no. 11, pp. 7571–7579, Nov. 2020.

[9] D. Deschrijver, F. Vanhee, D. Pissoort, and T. Dhaene, "Automated near-field scanning algorithm for the EMC analysis of electronic devices," *IEEE Trans. Electromagn. Compat.*, vol. 54, no. 3, pp. 502–510, Jun. 2012.

[10] O. Malyuskin and V. F. Fusco, "High-resolution microwave near-field surface imaging using resonance probes," *IEEE Trans. Instrum. Meas.*, vol. 65, no. 1, pp. 189–200, Jan. 2015.

[11] R. Rafiee Alavi, R. Mirzavand, A. Kiaee, and P. Mousavi, "An adaptive data acquisition technique to enhance the speed of near-field antenna measurement," *IEEE Trans. Antennas Propag.*, vol. 70, no. 7, pp. 5873–5883, Jul. 2022.

[12] W. Shao and Q. Chen, "Single-pixel scanning near-field imaging with subwavelength resolution using sharp focusing Mikaelian lens," *IEEE Trans. Microw. Theory Techn.*, vol. 71, no. 2, pp. 795–804, Feb. 2023.

[13] M. Azadifar, H. Karami, F. Rachidi, and M. Rubinstein, "A compressive sensing framework for EMI source localization using a metalens structure: Localization beyond the diffraction limit," *IEEE Trans. Electromagn. Compat.*, vol. 64, no. 1, pp. 58–65, Feb. 2022.

[14] M. H. Francis, "Aperture-sampling requirements [and reply]," *IEEE Antennas Propag. Mag.*, vol. 39, no. 5, pp. 76–81, Oct. 1997.

[15] F. D'Agostino et al., "Far-field pattern reconstruction from near-field data collected via a nonconventional plane-rectangular scanning: Experimental testing," *Int. J. Antennas Propag.*, vol. 2014, 2014, Art. no. 763687.

[16] J. Li, J. Zhou, S. Yong, S. Liu, and V. Khilkevich, "Automatic sparse ESM scan using Gaussian process regression," in *Proc. IEEE Int. Symp. Electromagn. Compat. Signal/Power Integrity*, 2020, pp. 671–675.

[17] Y. Liu and B. Ravelo, "Fully time-domain scanning of EM near-field radiated by RF circuits," *Prog. Electromagn. Res. B*, vol. 57, pp. 21–46, 2014.

[18] B. Zitouna and J. B. H. Slama, "Enhancement of time-domain electromagnetic inverse method for modeling circuits radiations," *IEEE Trans. Electromagn. Compat.*, vol. 58, no. 2, pp. 534–542, Apr. 2016.

[19] G. Ptitcyn, M. S. Mirmoosa, A. Sotoodehfar, and S. A. Tretyakov, "A tutorial on the basics of time-varying electromagnetic systems and circuits: Historic overview and basic concepts of time-modulation," *IEEE Antennas Propag. Mag.*, vol. 65, no. 4, pp. 10–20, Aug. 2023.

[20] S. Hedia, B. Zitouna, J. B. H. Slama, and L. Pichon, "Electromagnetic time reversal in the near field: Characterization of transient disturbances in power electronics," *IEEE Trans. Electromagn. Compat.*, vol. 62, no. 5, pp. 1869–1878, Oct. 2020.

[21] Y. Xie, X. Yang, P. Su, Y. He, and Y. Qiu, "A microwave time domain reflectometry technique combining the wavelet decomposition analysis and artificial neural network for detection of defects in dielectric structures," *IEEE Trans. Instrum. Meas.*, vol. 71, 2022, Art. no. 8001211.

[22] E. J. Candes and Y. Plan, "A probabilistic and ripless theory of compressed sensing," *IEEE Trans. Inf. Theory*, vol. 57, no. 11, pp. 7235–7254, Nov. 2011.

[23] J. D. Blanchard, C. Cartis, and J. Tanner, "Compressed sensing: How sharp is the restricted isometry property?," *SIAM Rev.*, vol. 53, no. 1, pp. 105–125, 2011.

[24] E. J. Candes and T. Tao, "Near-optimal signal recovery from random projections: Universal encoding strategies?," *IEEE Trans. Inf. Theory*, vol. 52, no. 12, pp. 5406–5425, Dec. 2006.

[25] G. Peyre, "Best basis compressed sensing," *IEEE Trans. Signal Process.*, vol. 58, no. 5, pp. 2613–2622, May 2010.

[26] D. Needell and J. A. Tropp, "CoSaMP: Iterative signal recovery from incomplete and inaccurate samples," *Appl. Comput. Harmon. Anal.*, vol. 26, no. 3, pp. 301–321, 2009.

[27] M. A. Oliver and R. Webster, "Kriging: A method of interpolation for geographical information systems," *Int. J. Geographical Inf. Sci.*, vol. 4, no. 3, pp. 313–332, 1990.

[28] H. Daud, M. N. M. Aris, K. A. M. Noh, and S. C. Dass, "A novel methodology for hydrocarbon depth prediction in seabed logging: Gaussian process-based inverse modeling of electromagnetic data," *Appl. Sci.*, vol. 11, no. 4, 2021, Art. no. 1492.

[29] A. A. Tesfay and L. Clavier, "Gaussian process-based spatial reconstruction of electromagnetic fields," 2022, *arXiv:2203.01869*.

[30] Z. Ying, "Asymptotic properties of a maximum likelihood estimator with data from a Gaussian process," *J. Multivariate Anal.*, vol. 36, no. 2, pp. 280–296, 1991.

[31] T. Karvonen and C. J. Oates, "Maximum likelihood estimation in Gaussian process regression is ILL-posed," *J. Mach. Learn. Res.*, vol. 24, no. 120, pp. 1–47, 2023.

[32] P. J. Schmid, "Dynamic mode decomposition of numerical and experimental data," *J. Fluid Mech.*, vol. 656, pp. 5–28, 2010.

[33] Y. Zhang, L. Jiang, and H. T. Ewe, "A novel data-driven modeling method for the spatial–temporal correlated complex sea clutter," *IEEE Trans. Geosci. Remote Sens.*, vol. 60, 2022, Art. no. 5104211.

[34] S. L. Brunton, B. W. Brunton, J. L. Proctor, E. Kaiser, and J. N. Kutz, "Chaos as an intermittently forced linear system," *Nature Commun.*, vol. 8, no. 1, 2017, Art. no. 19.

[35] Y. Zhang and L. Jiang, "Suppressing white-noise interference for orbital angular momentum waves via the forward–backward dynamic mode decomposition," *IEEE Trans. Antennas Propag.*, vol. 71, no. 3, pp. 2879–2884, Mar. 2023.

[36] Y. Zhang, M. L. N. Chen, and L. Jiang, "Extraction of the characteristics of vortex beams with a partial receiving aperture at arbitrary locations," *J. Opt.*, vol. 23, no. 8, Jul. 2021, Art. no. 085601, doi: 10.1088/2040-8986/ac0ff3.

[37] Y. Zhang and L. Jiang, "A novel demultiplexing scheme for vortex beams in radio communication systems," *IEEE Trans. Veh. Technol.*, vol. 70, no. 7, pp. 7243–7248, Jul. 2021.

[38] Y. Zhang, L. Jiang, and H.-T. Chou, "Data-driven scheme for joint estimation of direction-of-arrival and frequency with uniform linear array," *IEEE Trans. Veh. Technol.*, vol. 72, no. 12, pp. 15706–15718, Dec. 2023.

[39] Y. Zhang and L. Jiang, "A direct data approach to joint 2-D DOA and frequency estimation with l-shaped array," *IEEE Trans. Aerosp. Electron. Syst.*, vol. 59, no. 4, pp. 3684–3694, Aug. 2023.

[40] Y. Zhang and L. Jiang, "A novel data-driven method for two-dimensional angles finding via uniform rectangular array with automatic pairing," *IEEE Trans. Veh. Technol.*, vol. 72, no. 2, pp. 1972–1981, Feb. 2023.

[41] F. Andreuzzi, N. Demo, and G. Rozza, "A dynamic mode decomposition extension for the forecasting of parametric dynamical systems," *SIAM J. Appl. Dyn. Syst.*, vol. 22, no. 3, pp. 2432–2458, 2023.

[42] Y. Zhang and L. Jiang, "A novel data-driven analysis method for electromagnetic radiations based on dynamic mode decomposition," *IEEE Trans. Electromagn. Compat.*, vol. 62, no. 4, pp. 1443–1450, Aug. 2020.

[43] S. X. Ta, I. Park, and R. W. Ziolkowski, "Crossed dipole antennas: A review," *IEEE Antennas Propag. Mag.*, vol. 57, no. 5, pp. 107–122, Oct. 2015.

[44] J. Kulkarni, C.-Y.-D. Sim, and V. Deshpande, "Low-profile, compact, two port MIMO antenna conforming Wi-Fi-5/Wi-Fi-6/v2X/DSRC/InSAT-C for wireless industrial applications," in *Proc. IEEE 17th India Council Int. Conf.*, 2020, pp. 1–5.

[45] D. R. Aloori, "Simulation of near-field generated by S-band rectangular horn antenna array for hyperthermia therapy applications using 4NEC2 software," Ph.D. dissertation, Dept. Elect. Electron. Eng., California State Univ., Sacramento, CA, USA, 2010.

[46] "4NEC2," Accessed on: Jan. 10, 2023. [Online]. Available: https://www.qsl.net/4nec2/

[47] W.-L. Loh, "On Latin hypercube sampling," *Ann. Stat.*, vol. 24, no. 5, pp. 2058–2080, 1996.

[48] J. C. Helton and F. J. Davis, "Latin hypercube sampling and the propagation of uncertainty in analyses of complex systems," *Rel. Eng. Syst. Saf.*, vol. 81, no. 1, pp. 23–69, 2003.

[49] B. Van der Streeck et al., "Practical implementation of a sequential sampling algorithm for EMI near-field scanning," in *Proc. Int. Symp. Electromag. Compat. Eur.*, 2012, pp. 1–5.

[50] M. D. Migliore, "A compressed sensing approach for array diagnosis from a small set of near-field measurements," *IEEE Trans. Antennas Propag.*, vol. 59, no. 6, pp. 2127–2133, Jun. 2011.

[51] W.-J. Chang and T.-H. Fang, "An inverse method for determining the interaction force between the probe and sample using scanning near-field optical microscopy," *Phys. Lett. A*, vol. 348, no. 3, pp. 260–265, 2006. [Online]. Available: https://www.sciencedirect.com/science/article/pii/S0375960105013459